

Towards a Universal Veering Profile for Turbulent Ekman Flow at arbitrary Reynolds number - Part 2

LES and DNS of Turbulent Ekman Flow

Draft August 4, 2021

Abstract

An analytical formulation for the profiles of stream- and span-wise velocity in turbulent Ekman flow is analysed using large-eddy simulation. A comparison of a turbulent Ekman flow of $Re_D = 1600$ simulated by DNS and LES is shown.

1 Introduction

The same turbulent Ekman flow is simulated by DNS and LES and the results are compared.

Profile of wind direction from DNS - what can be learned from it for LES?

Limits of coarse resolution

Big Reynolds numbers \rightarrow LES

$$Re_D = GD/\nu, D = \sqrt{2\nu/f}, Re_D = G/\sqrt{\frac{1}{2}\nu f}$$

The velocity profiles of both horizontal components of the turbulent Ekman flow provide a benchmark test for LES model. \rightarrow First step towards a generic wind profile including stratification (and inversion?)?

2 A Universal Velocity Profile for the Turbulent Ekman Layer

The universal velocity profile for the turbulent Ekman layer consists of several parts for different layers of the boundary layer. Near the surface, viscous forces dominate the flow. In the middle part, the velocity profile has a logarithmic shape which passes over into an Ekman spiral. In the following, the distinct layers for both horizontal components of the velocity are described.

2.1 Total profile

From the layers of the velocity profile, a total profile for the whole boundary layer is formed. The profile of the stream-wise component of the velocity is separated into three layers, which are the viscous layer U_{visc} , the logarithmic layer U_{log} , and the Ekman layer U_{EK} . The span-wise component of the velocity is separated into two layers, namely the inner layer V_{inner} , and the Ekman layer V_{EK} .

$$U = (1 - w_{visc})U_{visc} + (w_{visc} - w_{outer})U_{log} + w_{outer}U_{EK}, \quad (1)$$

$$V = (1 - w_{outer})V_{inner} + w_{outer}V_{EK}. \quad (2)$$

The transition between consecutive layers is formed by a transfer function:

$$w_* = \frac{1}{2} \left(\operatorname{erf} \left[\sigma_T \log \left(\frac{z}{z_T} \right) \right] + 1 \right), \quad (3)$$

where σ_T is a transition scale that defines the width of the transition and z_T is the height of the transition, where the upper and the lower layer equally contribute to the velocity ($w_*(z_T) = 0.5$).

2.2 Drag-Law

The geostrophic drag $Z \equiv u_\star/G$ and the direction between the shear stress and the geostrophic wind α are two key parameters of the Ekman flow. They can be estimated using a semi-empirical drag-law based on Spalart [1989], which describes them as functions of only the Reynolds number:

$$\frac{G}{u_\star} \cos \phi^\star = \frac{1}{\kappa} \log Re_\tau + C - A_r, \quad (4a)$$

$$\sin \phi^\star = A_i \frac{u_\star}{G}, \quad (4b)$$

$$\alpha = \phi^\star - \frac{C_5}{Re_\tau}, \quad (4c)$$

with $Re_\tau = Re_D^2 \frac{u_\star^2}{G^2}$ (nach dem Python-Skript eher $Re_\tau = \frac{Re_D^2}{2} \frac{u_\star^2}{G^2}$?), $\kappa = 0.415$, $A_r = 4.80$, $A_i = -5.57$, $C = 5.4605$, $C_5 = -57.8$. This law is in excellent agreement with DNS in the range $400 \leq Re_D \leq 1600$ as demonstrated by Ansorge and Mellado [2014].

2.3 Stream-wise Velocity Component

In the viscous sublayer, the span-wise velocity is close to zero and the stream-wise velocity is described by the law of the wall:

$$U^{\alpha+} = z^+, \quad (5)$$

(the index α indicates the alignment with the direction of the shear stress). Around $z^+ = 5$, the velocity is beginning to deviate from its linear profile and the buffer layer forms the transition between viscous layer and logarithmic layer. From the surface up to the buffer layer, the stream-wise velocity is described by

$$U_{inner}^{\alpha+} = \frac{z^+ + \gamma_4(z^+)^4 + \gamma_6(z^+)^6}{1 + \gamma_6/u_{ref}(z^+)^6}, \quad (6)$$

where $\gamma_4 = -3.825 \cdot 10^{-4}$, $\gamma_6 = 6.32 \cdot 10^{-6}$, and $u_{ref} = 0.07825$.

The logarithmic region of the stream-wise velocity is

$$U_{\log}^{\alpha+} = \frac{1}{\kappa} \log z^+ + C, \quad (7)$$

where $\kappa = 0.416$, and $C = 5.4605$. The transition between buffer layer and logarithmic layer is located at $z_T^+ = 19$ with a scale $\sigma_T = 2$.

2.4 Profile in Outer Layer

Above the boundary layer, the horizontal pressure gradient is balanced by the coriolis force and the wind speed equals the geostrophic wind G . For the stationary case, the horizontal equations of motion can be written

$$0 = fV + \nu_e \partial_z^2 U, \quad (8a)$$

$$0 = -f(U - G) + \nu_e \partial_z^2 V, \quad (8b)$$

with the x-axis aligned with the geostrophic wind (What is ν_e ? Kind of eddy viscosity?). This is solved by

$$U_{EK} = G + A \exp^{-\tilde{z}} \cos \tilde{z}, \quad (9a)$$

$$V_{EK} = -A \exp^{-\tilde{z}} \sin \tilde{z}, \quad (9b)$$

Table 1: Key parameters of the simulated cases. f , ν , and G are input parameters while u_* and α are the expected results according to Spalart [1989]

Name	Re_D	Re_τ	f [s $^{-1}$]	ν [m 2 s $^{-1}$]	G [ms $^{-1}$]	u_* [ms $^{-1}$]	α [°]
Re1	10^3	$3 \cdot 10^3$	10^{-4}	$1.5 \cdot 10^{-5}$	0.0274	0.00144	18.96
Re2	$1.5 \cdot 10^5$	$7.3 \cdot 10^6$	10^{-4}	$1.5 \cdot 10^{-5}$	4.108	0.1048	8.51
Re3	10^6	$2.2 \cdot 10^8$	10^{-4}	$1.5 \cdot 10^{-5}$	27.39	0.5785	7.03

where $A = 8.4u_* - 150/\delta^+$, $\tilde{z} = (z - z_r)/D_E$, $z_r = 0.12\delta$, and $D_E = 3\delta/4\pi \approx 0.24\delta$. The parameters are deduced from DNS.

The transition from the logarithmic layer to the Ekman layer is located at $z^- = 0.3$ (talk: $z_T^- = 0.3 - 120/Re_D$) with a transition scale of $\sigma_T = 2$ for the stream-wise velocity.

2.5 Span-wise Velocity

For $z^+ \leq 10$, the knowledge on U^α is exploited to parametrize V^α in terms of direction:

$$\alpha_{visc} = \frac{C_1 + C_2(\log z^+)^2}{Re_\tau Z}, \quad (10)$$

$$\Rightarrow V_{visc}^\alpha = U^\alpha \tan(\alpha_{visc}), \quad (11)$$

where $C_1 = 40$, $C_2 = 26$, and $Z = u_*/G$ (not valid for $z^+ < 1!$?). Above $z^+ = 10$, V^α is continued with

$$V_{inner}^\alpha = V_{10}^\alpha + A \log\left(\frac{z^+}{10}\right) + B(z^+ - 10), \quad (12)$$

which matches the value of $V_{10}^\alpha = V_{visc}^\alpha(z^+ = 10)$. To also match the gradient $m_{10} = \partial V_{visc}^\alpha / \partial z^+$ at $z^+ = 10$ and the value of V_{EK}^α at $z^- = 0.27$, the values of A and B need to be

$$A = \frac{V_{EK}^\alpha(z^- = 0.27) - V_{10}^\alpha - m_{10}(0.27z^+/Re_\tau - 10)}{\log(0.27z^+/(10Re_\tau)) - (0.27z^+/Re_\tau - 10)/10}, \quad (13)$$

$$B = m_{10} - A/10. \quad (14)$$

At $z_T^- = 0.27$, V_{inner}^α is blended into V_{EK}^α .

3 Setup

3.1 Settings

An incompressible, turbulent Ekman flow over a flat rotating plate is simulated for three different Reynolds numbers $Re_D = 10^3; 1.5 \cdot 10^5; 10^6$, hereafter $Re1$, $Re2$, and $Re3$, respectively. The key input parameters of the three cases are presented in table 1.

The domain is rotating around the z-axis with an angular velocity such that the Coriolis parameter is $f = 10^{-4}$. The stratification of the flow is entirely neutral, i.e., the potential temperature $\Theta = const.$ for the whole domain. At the upper boundary, a no-penetration boundary condition is used and the horizontal components of the wind are forced to be equal to the geostrophic wind. At the bottom, a constant flux layer is assumed and the Monin-Obukhov Theory (MOST) is used to calculate the surface momentum fluxes $\overline{u''w''}_0$ and $\overline{v''w''}_0$.

To study the effect of resolution on the simulations, three different grid resolutions are chosen for each Reynolds number case. The grid cell sizes are around $\delta/50$, $\delta/100$, and $\delta/150$ for a coarse, a medium, and a fine resolution, respectively (see table 2).

The grid spacing inside of the boundary layer is isotropic up to the height $\delta = u_*/f$, from where on the grid spacings in z-direction are stretched with the factor 1.02 each level, up to

Table 2: Simulations and grid parameters

Name	Δ [m]	$n_x = n_y$	n_z	L_x [m]	L_z [m]
R1_150	0.14	1536	288	215.04	122
R1_100	0.2	1080	192	216	67.6
R1_50	0.4	576	120	230.4	78.3
R2_150	7	1536	288	10752	3937
R2_100	10	1080	192	10800	3414
R2_50	20	576	120	11520	6212
R3_150	40	1536	240	61440	21600
R3_100	55	1080	192	59400	18687
R3_50	110	576	120	63360	6212

a maximum grid spacing of $6\Delta x$. The number of vertical grid points is chosen such that the domain height is at least three times δ . Above two thirds of the total domain, Rayleigh damping is active to avoid reflections from the upper boundary.

In part I of this publication, the DNS of low Reynolds number simulations ($Re_D \leq 1600$) have a horizontal domain length of $L_x = 0.54G/f$ or $L_x = 1.08G/f$ (reason?). For these Reynolds numbers, u_*/G is around 0.05 so $L_x = 0.54G/f \approx 10u_*/f = 10\delta$ (introduce δ_{95} as boundary layer height?). However, u_*/G decreases with increasing Reynolds number and is around 0.02 for $Re_D = 10^6$. A domain size of half the Rossby radius would then extend to $L_x \approx 25\delta$. Such a large domain would imply immense computational costs. To avoid this, the horizontal domain length was chosen to be $L_x \approx 10\delta$ for all Reynolds numbers, which is $L_x/(G/f) \approx 0.48, 0.25, 0.22$ for $Re1, Re2$, and $Re3$, respectively. An overview over the parameters of the settings is presented in table 2.

As LES uses a much coarser resolution than DNS, unresolved processes like the turbulent transport on the subgrid scale need to be modeled by a subgrid-scale model (SGS model). The model code of PALM offers two different SGS models: a 1.5-order closure after Deardorff [1980] and a dynamic closure after Heinz [2008]. For most of the simulations, the 1.5-order closure is used, but several simulations are repeated using the dynamic closure for comparison.

The problem is solved using a three-step Runge-Kutta method. For scalar advection a 5th order Wicker-Skamarock scheme is employed. A comprehensive description of the LES model is given by Maronga et al. [2020a].

3.2 Correction of Mean Velocity

The initial profile of the flow is calculated by a 1d-model with a Reynolds-average based turbulence parametrization. At the beginning of the 3d run, random perturbations are imposed to the horizontal velocity field to trigger the evolution of turbulent eddies. The following imbalance between pressure force and coriolis force results in an inertial oscillation of the period $T_{io} = 2\pi/f$. The oscillation slowly decays over time and eventually vanishes. To avoid an overly long spin-up time, an ensemble average of the horizontal wind profiles $\langle U \rangle(z)$ and $\langle V \rangle(z)$ is taken over a period of $T_{avg} = T_{io}$ after an evolution of turbulence for $T_{spin-up} = T_{io}/2$. At the point in time $t = \frac{3}{2}T_{io}$, the momentary wind field is adjusted such that the instantaneous domain-averaged wind profiles $\bar{U}(z)$ and $\bar{V}(z)$ are shifted to the values of the ensemble average over a whole inertial period:

$$u_{ijk}^{new} = u_{ijk} - \bar{U}_k + \langle U \rangle_k, \quad (15)$$

where i and j indicate the horizontal grid points and k indicates the vertical grid point. After this transformation of the flow field, the inertial oscillation is nearly gone and the simulation is continued for another period T_{io} to collect data for the evaluation. The effect of this correction

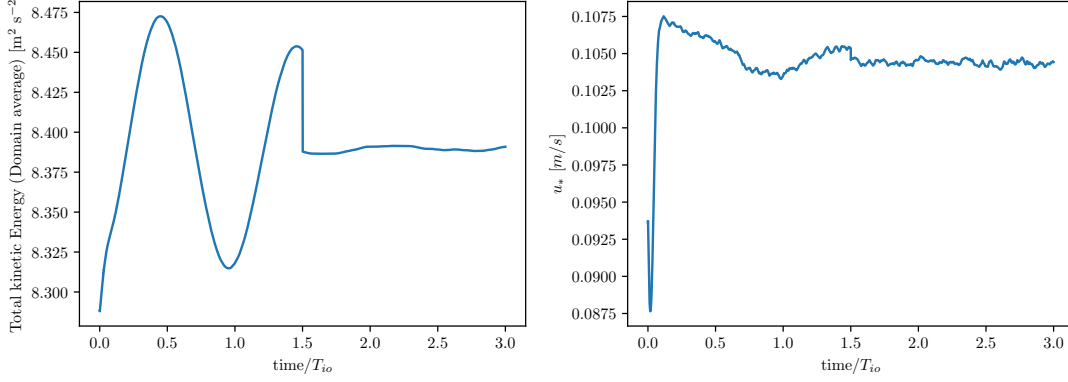


Figure 1: Left: domain-averaged kinetic energy of the simulation Re2_100. Right: horizontal average of the friction velocity

of the mean velocity on the inertial oscillation is shown in fig. 1. **this procedure seems to work better for low Reynolds numbers and coarse resolutions**

3.3 Choice of z_0

In contrast to DNS, the viscosity of the fluid hardly influences the flow on the grid scale of the LES, so the terms in the Navier-Stokes equation containing ν are neglected and only the Euler equations are solved. Instead of a no-slip condition at the bottom, a constant flux layer is assumed below the first grid point and the Monin–Obukhov theory is used to compute the friction velocity and the stresses at the first grid point:

$$u_\star = \frac{\kappa(U^2 + V^2)^{0.5}}{\ln(z/z_0)}, \quad (16)$$

$$-\overline{u''w''}_0 = \frac{\kappa U u_\star}{\ln(z/z_0)}. \quad (17)$$

Nevertheless, the viscosity is taken into account indirectly by choosing the roughness length z_0 . This becomes clear by considering the law of the wall for a smooth surface:

$$u^+ = \frac{1}{\kappa} \ln(z^+) + C^+ = \frac{1}{\kappa} \ln\left(\frac{z^+}{z_0^+}\right) \quad (18)$$

with $\kappa \approx 0.416$ and $C^+ \approx 5.4605$ for a smooth wall (reference?). This leads to

$$z_0^+ = \exp(-\kappa C^+) \approx 0.1, \quad (19)$$

which is the roughness length for a smooth wall in inner units. So the roughness length in SI-units $z_0 = z_0^+ \nu / u_\star \approx 0.1 \nu / u_\star$ depends on the viscosity of the fluid, which means that the choice of z_0 is equivalent (?) to a choice of the viscosity ν .

The choice of z_0 and the turbulent flow (driven by the geostrophic wind G) determine the magnitude of u_\star in a non trivial way. As will be demonstrated below, the choice of $z_0 = 0.1$ does not lead to the expected value of u_\star predicted by Spalart. To reproduce the predicted $u_{\star pred}$, a sensitivity study was performed whose results are shown in fig. 2. A variation of z_0^+ showed that the resulting u_\star follow a power law $u_\star / u_{\star pred} = a(z_0^+)^m$. In order to get the expected friction velocity, z_0^+ had to be 0.149, 0.174, and 0.196 for the cases Re1, Re2, and Re3, respectively. This is a quite strong dependence on the Reynolds number. **Can we explain this?**

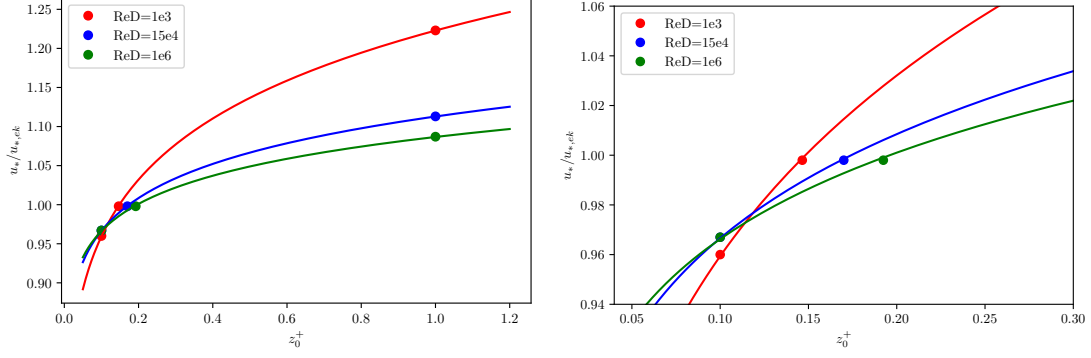


Figure 2: The friction velocity as function of the roughness length with fit

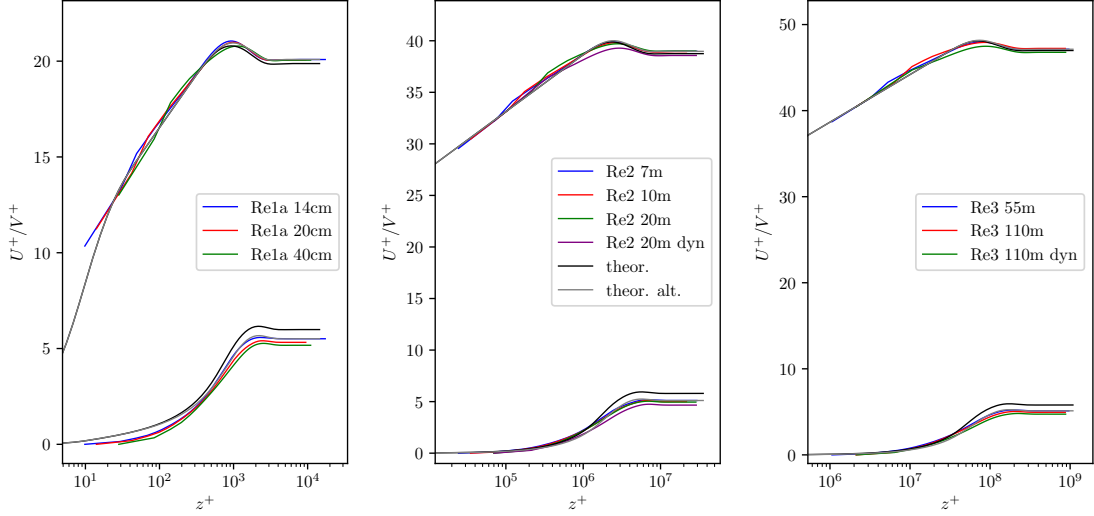


Figure 3: Shear-aligned profiles in inner scaling

4 Results

The turbulent structures in boundary layers of high Reynolds numbers extend over a large range of scales. For the description of their vertical mean profiles, inner units ($z^+ = zu_*/\nu$, $U^+ = U/u_*$) and outer units ($z^- = z/\delta$, $U^- = U/G$) are used. At the lower boundary, the x-axis of the inner units is aligned with the shear stress, whereas the x-axis of the outer units is aligned with the geostrophic wind. The angle between both axes is called α .

A principal idea behind LES is to neglect the small scales of the flow and resolve only the large eddies, which carry most of the turbulent kinetic energy. Hence, the viscous sublayer and the buffer layer are not resolved by LES and cannot be compared. The first grid point of an LES usually lies inside of the logarithmic region of the boundary layer. Furthermore, the flow is usually underresolved in the lower layers of an LES, since near the bottom, the vertical component is massively restricted by the non-permeability of the wall.

4.1 Logarithmic layer stream-wise velocity

Figure 4 shows $\kappa = z^+ \partial U^+ / \partial z^+$, which is constant in the logarithmic layer. The theoretical profile shows a constant κ up to $z^- \approx 0.1$ for the case Re1 and up to $z^- \approx 0.15$ for the cases Re2 and Re3. All cases have in common that an increase in resolution leads to a profile much closer to the theoretical curve.

A typical feature of LES is the log-layer mismatch of the first grid points above the bottom,

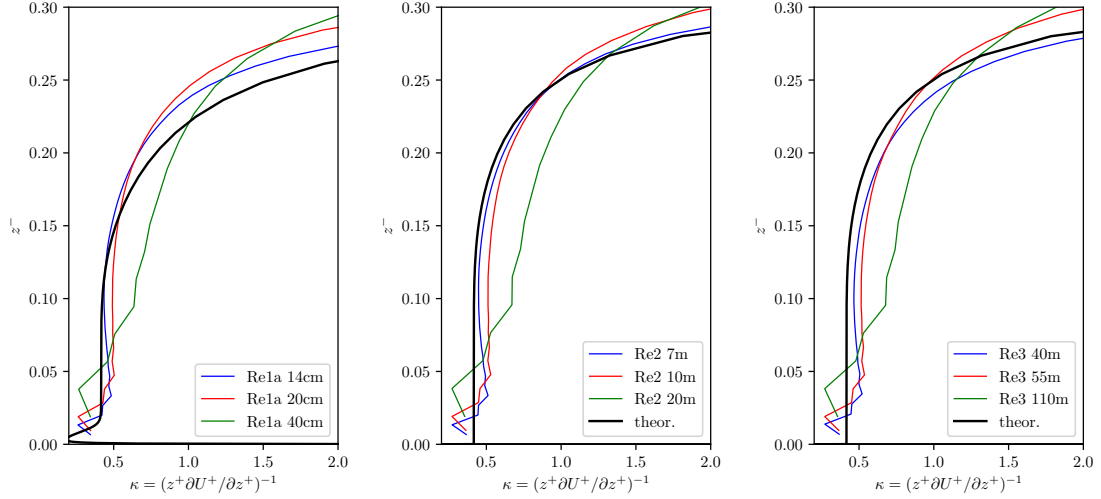


Figure 4: κ in the logarithmic region and above for different Reynolds numbers and resolutions

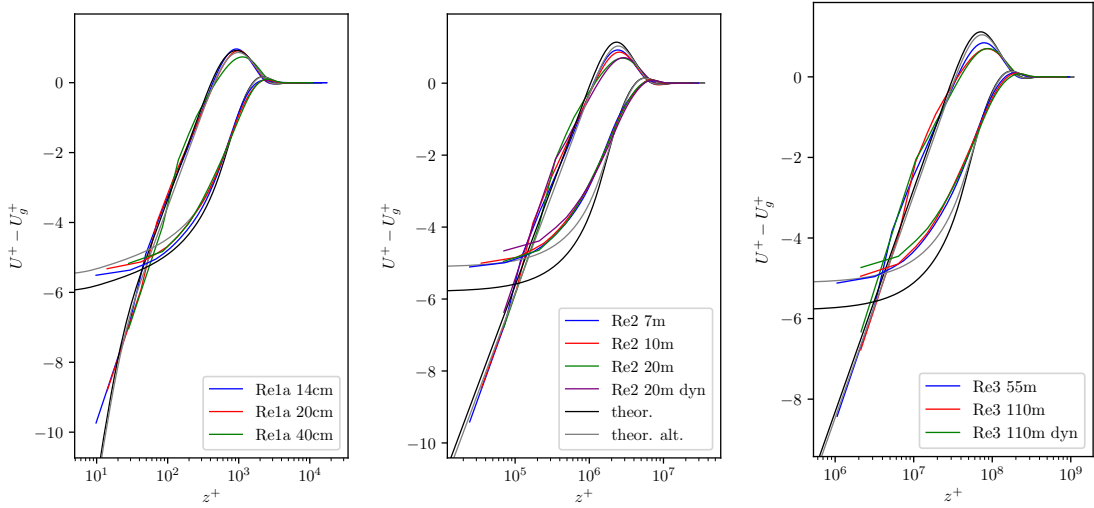


Figure 5: Shear-aligned velocity deficit

comprehensively discussed by Brasseur and Wei [2010]. According to Maronga et al. [2020b], mean profiles follow MOST at height levels starting from the seventh grid above the surface.

An obvious feature of the low Reynolds number case is that the viscous sublayer represents a notable share of the boundary layer, while this layer is hardly visible for the high Reynolds number cases.

A Reynolds number of $Re_D = 1600$ is a very unusual Reynolds number for an LES. The first grid point of the LES lies at $\Delta/2$ and should lie in the logarithmic region of the boundary layer (citation?). For the finer resolved simulations of the low Reynolds number, the first grid point lies well in the buffer layer or even in the viscous sublayer. That means that the simulation results of this point are unlikely to produce reasonable results since an LES does not comprehend the physics needed to describe the behavior of the flow in this region.

The transition from buffer layer to logarithmic layer lies around $z^+ = 19$. The first grid point of the simulation *Re1* lies at $z^+ = 14$ for the 20 cm resolution and at $z^+ = 10$ for the 14 cm resolution.

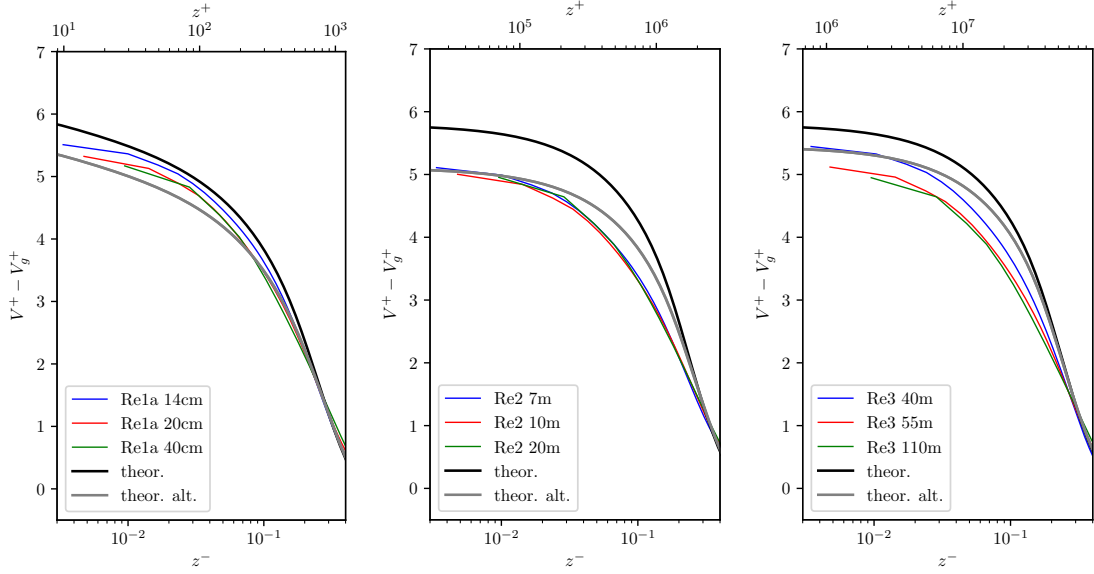


Figure 6: Shear-aligned velocity deficit of the v-component in the logarithmic layer

4.2 Logarithmic layer span-wise velocity

Figure 6

4.3 Ekman layer

Hodograph: in reality (or DNS), the wind profile shows only a very little change of wind direction near the bottom, whereas LES starts veering from the first grid point on.

For the case Re1, the curves for all resolutions fall quite well onto the theoretical hodograph. For the cases Re2 and Re3, the hodographs clearly show that the veering is underestimated by the LES.

There is a clear tendency that finer resolutions lead to a bigger α which is strongest for case Re3. Nevertheless, the predicted α is reached by non of the LES.

The adaption of the theoretical curve by using the α from the fines LES seems to be beneficial only for high Reynolds numbers. α is defined as the direction of the wind at the bottom while in LES we only have the direction of the wind at the first grid point: further veering below the first grid point is not taken into account. For high Reynolds numbers, the direction of the flow stays almost constant for a much wider part of the boundary layer (around 1% for Re2 and Re3), while for lower Reynolds number, the direction changes significantly much earlier (around 0.1% for Re1). The total α predicted by the theoretical profile (and the DNS) is 16.8° and the α of the LES with finest resolution of case Re1 is 15.3° . Despite this considerable difference, the curves match quite well and LES reproduces the correct course of wind directions at all heights above the first grid point.

Limits of coarse resolution - where is the MOST-Point in Hodograph?

Vergleich SGS-Modelle

As stated before, eq. 4 is very well validated for the range $400 < Re_D < 1600$ [Ansorge and Mellado, 2014]. For Reynolds numbers like $Re_D = 1.5 \cdot 10^5$ or even $Re_D = 10^6$, there exist neither DNS nor experimental data. Hence, the solutions of eq. 4 are not to be taken as certainly correct and one might assume that the LES solution is not definitively incorrect. This being said, the theoretical profiles are recalculated with the values of u_\star and α from the LES solution.

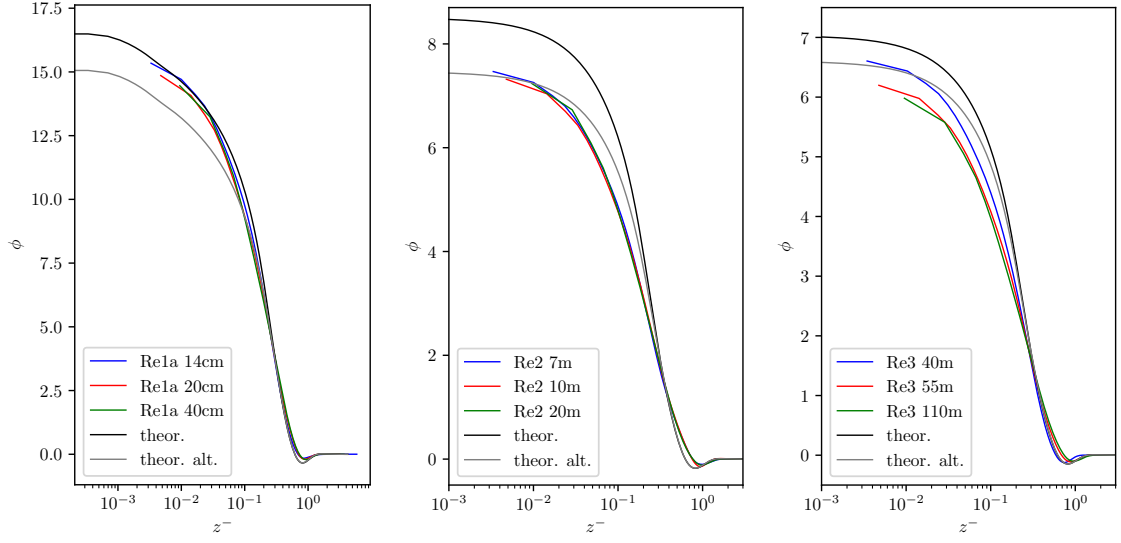


Figure 7: Direction of the mean flow with respect to the geostrophic wind.

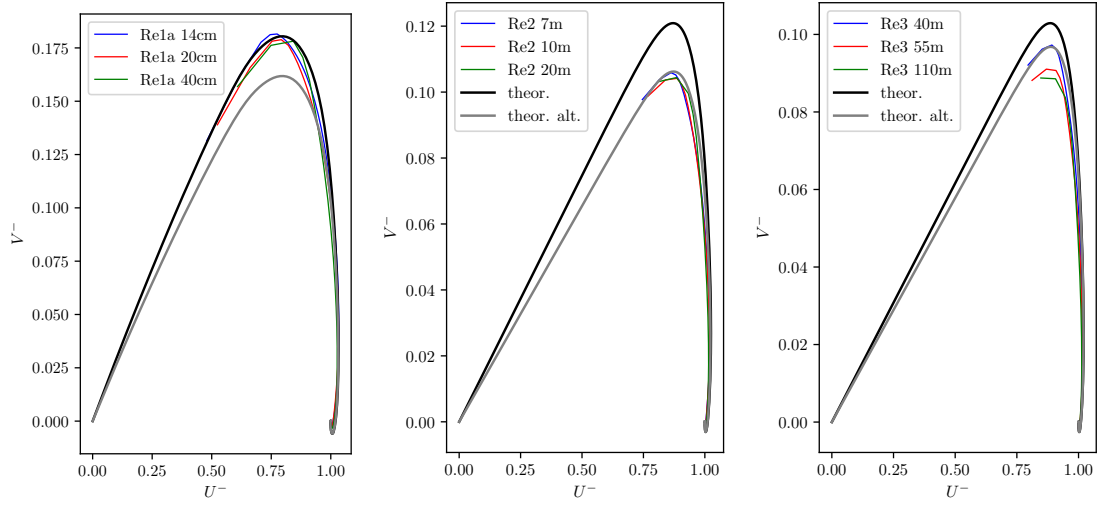


Figure 8: Geostrophy aligned hodograph

5 Discussion and Conclusions

Interesting comparison between DNS and LES

Overall: good fit between theoretical profile and LES

Resolution of LES matters a lot

Helpful for rating LES profile: height where profile should deviate from logarithmic shape.

Theoretical profiles provide a very detailed benchmark for all aspects of the flow. A very good hit of the hodograph might coincide with a poor curve for κ .

References

- Cedrick Ansgorge and Juan Pedro Mellado. Global intermittency and collapsing turbulence in the stratified planetary boundary layer. *Boundary-layer meteorology*, 153(1):89–116, 2014.
- James G Brasseur and Tie Wei. Designing large-eddy simulation of the turbulent boundary layer to capture law-of-the-wall scaling. *Phys Fluids*, 22(2):021303, 2010.
- James W Deardorff. Stratocumulus-capped mixed layers derived from a three-dimensional model. *Boundary-Layer Meteorology*, 18(4):495–527, 1980.
- Stefan Heinz. Realizability of dynamic subgrid-scale stress models via stochastic analysis. *Monte Carlo Methods Appl*, 14(4):311–329, 2008.
- Björn Maronga, Sabine Banzhaf, Cornelia Burmeister, Thomas Esch, Renate Forkel, Dominik Fröhlich, Vladimir Fuka, Katrin Frieda Gehrke, Jan Geletič, Sebastian Giersch, et al. Overview of the palm model system 6.0. *Geoscientific Model Development*, 13(3):1335–1372, 2020a.
- Björn Maronga, Christoph Knigge, and Siegfried Raasch. An improved surface boundary condition for large-eddy simulations based on monin–obukhov similarity theory: evaluation and consequences for grid convergence in neutral and stable conditions. *Boundary-Layer Meteorology*, 174(2):297–325, 2020b.
- Philippe R Spalart. Theoretical and numerical study of a three-dimensional turbulent boundary layer. *Journal of Fluid Mechanics*, 205:319–340, 1989.